



This is a repository copy of *High-Performance Multilayer Encapsulation for Perovskite Photovoltaics*.

White Rose Research Online URL for this paper:
<http://eprints.whiterose.ac.uk/134370/>

Version: Accepted Version

Article:

Wong-Stringer, M., Game, O.S., Smith, J.A. et al. (10 more authors) (2018)
High-Performance Multilayer Encapsulation for Perovskite Photovoltaics. *Advanced Energy Materials*, 8 (24). 1801234. ISSN 1614-6832

<https://doi.org/10.1002/aenm.201801234>

This is the peer reviewed version of the following article: M. Wong-Stringer, O. S. Game, J. A. Smith, T. J. Routledge, B. A. Alqurashy, B. G. Freestone, A. J. Parnell, N. Vaenas, V. Kumar, M. O. A. Alawad, A. Iraqi, C. Rodenburg, D. G. Lidzey, *Adv. Energy Mater.* 2018, 1801234, which has been published in final form at <https://doi.org/10.1002/aenm.201801234>. This article may be used for non-commercial purposes in accordance with Wiley Terms and Conditions for Self-Archiving.

Reuse

Items deposited in White Rose Research Online are protected by copyright, with all rights reserved unless indicated otherwise. They may be downloaded and/or printed for private study, or other acts as permitted by national copyright laws. The publisher or other rights holders may allow further reproduction and re-use of the full text version. This is indicated by the licence information on the White Rose Research Online record for the item.

Takedown

If you consider content in White Rose Research Online to be in breach of UK law, please notify us by emailing eprints@whiterose.ac.uk including the URL of the record and the reason for the withdrawal request.



eprints@whiterose.ac.uk
<https://eprints.whiterose.ac.uk/>

High performance Multi-Layer Encapsulation for Perovskite Photovoltaics

Michael Wong-Stringer¹, Onkar S. Game¹, Joel A. Smith¹, Thomas J. Routledge¹, Bakhet A. Alqurashy², Benjamin G. Freestone¹, Andrew J. Parnell¹, Naoum Vaenas¹, Vikas Kumar³, Majed O. A. Alawad⁴, Ahmed Iraqi⁴, Cornelia Rodenburg³ and David G. Lidzey^{1,5*}

¹Department of Physics & Astronomy, University of Sheffield, Hicks Building, Hounsfield Road, Sheffield, S3 7RH, UK

²Department of Basic Science and Technology, Community Faculty, Taibah University, 30002 Al-Madina Al-Mounawara, Saudi Arabia

³Department of Materials Science and Engineering, University of Sheffield, Mappin St, Sheffield, S1 3JD, UK

⁴Department of Chemistry, University of Sheffield, Brook Hill, Sheffield, S3 7HF, UK

⁵Ossila Limited, Windsor Street, Sheffield, S4 7WB, UK

*Corresponding author, email d.g.lidzey@sheffield.ac.uk

Keywords: PVP, epoxy, perovskite solar cells, stability, lifetime, T80, encapsulation, solvent anneal

Abstract

We have developed an encapsulation system comprising of a UV-curable epoxy, a solution-processed polymer interlayer and a glass cover-slip which we use to increase the stability of methylammonium lead triiodide ($\text{CH}_3\text{NH}_3\text{PbI}_3$) perovskite PV devices fabricated using a planar inverted architecture. We find this encapsulation system acts as an efficient barrier to extrinsic degradation processes (ingress of moisture and oxygen), and that the polymer acts as a barrier that protects the PV device from the epoxy before it is fully cured. This results in devices that maintain 80% of their initial power conversion efficiency after 1000 hours of AM1.5 irradiation. Such devices are used as a benchmark and are compared with devices having initially enhanced efficiency as a result of a solvent annealing process. We find that such solvent-annealed devices undergo enhanced burn-in and have a reduced long-term efficiency; a result demonstrating that initially enhanced device efficiency does not necessarily result in long-term stability.

The power conversion efficiency (PCEs) of perovskite solar cells (PSCs) fabricated using various process routines now routinely exceed 20%^[1-7], with a highest certified PCE reported being 22.7%^[7]. Such enhanced efficiency results from both detailed device optimisation studies and materials engineering. Perhaps the most significant development has been the introduction of inorganic cations (including potassium, caesium and rubidium) into the more ubiquitous methylammonium (CH_3NH_3^+) and formamidinium ($\text{HC}(\text{NH}_2)_2^+$) based perovskites. Such cations can result in a range of effects, including enhanced perovskite crystal growth,^[6] enhanced material stability at elevated temperature,^[4,6] and suppressed light-induced ion migration or segregation.^[5,8,9] Further enhancements in device stability have been gained from the use of thinner, hydrophobic, UV stable and dopant-free electron and hole transport materials (ETMs and HTMs).^[10-17] For example titanium dioxide (TiO_2) has been replaced by tin dioxide (SnO_2),^[10,18,19] which has reduced UV sensitivity, and the water soluble and acidic material poly(3,4-ethylenedioxythiophene) polystyrene sulfonate (PEDOT:PSS)^[2,20] has been replaced by hydrophobic polymers such as poly[bis(4-phenyl)(2,5,6-trimethylphenyl)amine] (PTAA) or poly(N,N'-bis-4-butylphenyl-N,N'-bisphenyl)benzidine (poly-TPD). Other work has explored reducing trap state density and enhancing charge transport across interfaces within a PSC device.^[1-6,21-24] Such progress indicates that with careful design, PSCs have the capability to achieve not only high PCE, but also acquire long-term stability.

An important component of PV is its encapsulation, as this protects it from the damaging effects of oxygen and moisture. In silicon-based PV, this is typically achieved using glass together with laminated ethylene vinyl acetate (EVA) layers. However this level of protection is not sufficient for PSCs and it is believed that perovskites are sensitive to decomposition products of EVA (acetic acid).^[25] For this reason, there is a clear need to develop effective encapsulation strategies for PSCs and to explore their role in extending the operational lifetime of the device. Indeed, effective encapsulation systems permit the study of intrinsic cell degradation mechanisms, such as those caused by light, temperature and processing route without unwanted effects resulting from moisture-induced degradation.

PV T80 device lifetime is defined as the time taken over which the PCE falls to 80% of its initial value.^[26,27] In our previous work on organic PCDTBT-based bulk heterojunction solar cells, we demonstrated that the use of a glass cover-slip and a UV curable epoxy can protect the device to such an extent that T80 lifetimes (measured after an initial burn-in) exceeding 10,000 hours can be demonstrated.^[26,28] We have also applied this encapsulation technique to PSCs, and concluded that the relatively short T80 lifetimes determined (280 hours after burn-in) resulted from the acidic^[29] and hydrophilic nature of the PEDOT:PSS hole extraction layer that was used.^[27] During this study however, it became apparent that some degradation occurred to the PSC during the UV curing of the epoxy, and it was speculated that either some polar solvent or initiators in the epoxy underwent a

reaction with the perovskite. We note that other work using UV curable epoxies to encapsulate PSCs has also not demonstrated devices having long-term stability.^[30–32]

In this paper, we demonstrate that perovskites can be degraded by the deposition and curing of typical epoxy materials. To mitigate this effect, we use a solution-processable polymer interlayer (polyvinylpyrrolidone (PVP)) placed between the PSC and the epoxy, which we demonstrate reduces direct degradation from the epoxy. This allows us to establish a significantly improved yield of high-performing, stable PSCs, with devices having a T80 lifetime of 1000 hours. Using our most stable process as a ‘baseline’, we then explore the effect of a solvent-annealing process that is often used to enhance device efficiency. Interestingly, we find that solvent annealed devices suffer from a large negative burn-in, such that 40% of their initial PCE is lost within the first 10 hours of aging under AM1.5 illumination. Our measurements demonstrate that devices must be separately optimised for efficiency and stability, and that efficient PSC devices are not necessarily operationally stable.

Devices were based on an indium tin oxide (ITO)/poly-TPD(F4-TCNQ)/MAPbI₃/PC₆₀BM/Bphen architecture and were fabricated as illustrated schematically in Figure 1a,b. Here, all layers (except the 100 nm thick silver cathode) were deposited by spin-coating. We have used the hydrophobic hole-transport polymer poly-TPD, doped with 2,3,5,6-Tetrafluoro-7,7,8,8-tetracyanoquinodimethane (F4-TCNQ). The use of such materials is expected to minimise the level of trapped moisture within the device. The MAPbI₃ perovskite was deposited by spin-coating from the low boiling-point, non-toxic solvent acetonitrile. Here, the perovskite ink was created by bubbling methylamine through an acetonitrile solution containing MAPbI₃ nanocrystals. During the bubbling the nanocrystals dissolve, forming a yellow-coloured solution. This solvent system was originally developed by Noel *et al*, and allows facile wettability of the perovskite precursor ink onto a poly-TPD surface.^[33] We acknowledge other reported techniques to improve wettability such as UV ozone treatments,^[34] dimethylformamide (DMF) rinsing^[35] and the use of ultra-thin amphiphilic polymer layers in order to increase the wettability of DMF-based perovskite solutions.^[36,37] However, we find that using MAPbI₃ deposited from an acetonitrile solution is a highly reproducible and reliable route to deposit perovskite layers on thin (<10nm) hydrophobic HTMs. Finally, PC₆₀BM and bathophenanthroline (BPhen) layers were deposited from chlorobenzene and IPA solutions respectively.

We have used our device architecture to explore the use of solvent annealing to grow perovskite grain size and thereby improve device efficiency. This process involves exposing the perovskite to a solvent vapour at an elevated temperature (100°C). This establishes a quasi-stable liquid-phase environment between the polar solvent dissolving the MAPbI₃ surfaces and grain boundaries, permitting the growth of perovskite grains.^[38] This process continues until the growth of larger grains is no longer energetically favourable - for example when the grain extends throughout

the entire film and can no longer maximise its surface area at the base and top of the film^[39]. To incorporate solvent annealing into the device preparation process, we held freshly prepared ITO/poly-TPD(F4-TCNQ)/MAPbI₃ multilayers at 100°C for 15 minutes in a dimethylformamide (DMF) solvent atmosphere. Following this, they were further annealed under nitrogen to remove any residual DMF, after which device processing proceeded as normal. We henceforth refer to solvent annealed and non-solvent annealed films as SA and non-SA respectively. We can evidence the growth of perovskite grains following solvent annealing using scanning electron microscopy as shown in Figure 2a,b (images recorded before and after solvent annealing). Here, it can be seen that the average size of MAPbI₃ grains increased from (140 ± 10) nm to (370 ± 30) nm following solvent annealing. This increase in grain size is also accompanied with an increase in surface roughness from 6.5 nm to 19 nm (calculated from AFM images presented in Figure S1).

We have characterised all devices using current-voltage (*J-V*) sweeps, together with stabilised power outputs (SPOs) (see example data for SA and non-SA devices in Figure 1c,d). Very little hysteresis is observed in the *JV* scan, as has been reported for other comparable inverted architecture PSCs.^[2] Full device metrics (PCE, J_{SC} , open-circuit voltage (V_{OC}) and fill factor (FF)) for ‘champion’ PSCs are shown in Table 1. We find that non-SA PSCs have a FF of 80% but have a lower J_{SC} of ~18 mA/cm², yielding a maximum PCE of 15.3%. As expected, SA PSCs had a PCE of 17.6%, explained largely as a result of their higher J_{SC} (20 mA/cm²). Here, we attribute the initially larger values of device J_{SC} in SA films to a reduction in the density of grain boundaries^[38,40,41]. However, we cannot exclude the possibility that increased light scattering (from a rougher top surface) or increased interface area between the MAPbI₃ and PC₆₀BM might also result in increased charge generation and extraction.

Devices were finally encapsulated in a nitrogen atmosphere using a one-part epoxy resin incorporating a UV-activated initiator (supplied by Ossila Ltd). Encapsulation involved placing a drop of epoxy on top of the device to create a seal over the whole PSC with a glass cover-slip, with the UV-epoxy being ‘cured’ by exposure to a UV lamp. Here, the epoxy is deposited such that it covers the PSC to the edge of substrate, and had a thickness of (70 ± 10) μm. This created a seal that is just over 2 mm between the edge device active-area and the surrounding atmosphere. Typical epoxies similar to the one employed here have a water vapour transmission rate (WVTR) of 0.7 – 0.94 g mm / m² day.¹ Permeability and Other Film Properties of Plastics and Elastomers, by William Woishnis, Published 1995 by Plastics Design Library, ISBN 1-884207-14-6¹ Alternately, a (135 ± 5) nm layer of the polymer PVP dissolved in methanol (see chemical structure in Figure 3e) was first spin-cast onto the device, after which the device was sealed using epoxy and glass. Here, PVP was selected as it can be processed from methanol, which due to its low boiling point (65°C) evaporates rapidly during spin-coating, leaving very little time for it to interact with the PSC stack. Note that control experiments have shown (see Figure S2a) that the exposure of MAPbI₃ PSCs to methanol does not affect their

electronic properties. A schematic of an encapsulated device is shown in Figure 1b.

We now examine the interaction between the epoxy and the different materials within the PSC device stack. Figure 3a shows comparative UV-Vis absorbance spectra of a control MAPbI₃ film on a quartz substrate, and a MAPbI₃ film that has been encapsulated using epoxy and glass. It can be seen that the unencapsulated MAPbI₃ control is characterised by a strong absorbance over the whole UV-Vis region with a sharp band edge around 780 nm. The absorbance of the encapsulated MAPbI₃ film is however reduced by more than a factor of three. This reduced absorption is clearly indicative of undesirable chemical reactions between the epoxy and MAPbI₃. We expect however that in a full PSC device stack, the perovskite layer would be partially protected from direct contact with the epoxy by the PC₆₀BM and silver electrodes.

To explore possible interactions between the epoxy and the PC₆₀BM, we have again measured changes in its relative UV-Vis absorption on encapsulation. We plot the absorbance spectrum of a pure PC₆₀BM film in Figure 3b, together with that of an encapsulated PC₆₀BM film. Here, the absorption of the epoxy encapsulation has been subtracted, as it is strongly absorbing at wavelengths < 450 nm. Again, we find a significant reduction in the absorption of the PC₆₀BM film on encapsulation; a result indicative of chemically-induced degradation. While the exact origin of this degradation mechanism is unclear, we suspect that either a photo-initiator or a polar-species within the epoxy reacts with the MAPbI₃ and PC₆₀BM during UV-curing, causing them to undergo decomposition. We believe that this degradation process is unlikely to result from direct UV-induced photo-oxidation, as the curing process was performed in a nitrogen atmosphere. We found that a multi-layer of perovskite/PC₆₀BM still loses some absorption if encapsulated with an epoxy that had been left under vacuum for 48 hours (Figure S3). This suggests that it is a component of the epoxy itself (such as a photo-initiator) that is most likely responsible for the degradation rather than absorbed moisture within the epoxy.

To demonstrate that the PVP polymer is able to protect the active layers within the device from chemical species present in the epoxy during curing, we repeated the encapsulation experiments described above. Here, PVP was first coated onto a film of PC₆₀BM. The results of this experiment are shown in Figure 3b, where it can be seen that the presence of the PVP coated onto the PC₆₀BM almost completely protects it from the effects of the epoxy, with the absorption of the PC₆₀BM being very similar in both the control and epoxy/PVP/PC₆₀BM films. Figure 3c similarly compares the absorption of a MAPbI₃/PC₆₀BM control, together with a MAPbI₃/PC₆₀BM/epoxy multilayer in which a PVP protection layer was either present or absent. Interestingly, we find that the absorption of the MAPbI₃/PC₆₀BM/epoxy multilayer is significantly reduced compared to the MAPbI₃/PC₆₀BM control, however the combined presence of the PVP/PC₆₀BM layers appears to completely protect the MAPbI₃ from damaging species within the epoxy. This protection can be clearly visualised in the images

shown in Figure 3d. Here, a bleaching of the MAPbI₃ absorption can be seen in devices that did not incorporate the PVP interlayer.

We now discuss the effect of the PVP interlayer on device efficiency and stability. Here, we have measured J - V sweeps and SPOs of PSCs that were recorded before encapsulation, after encapsulation and after 200 hours of aging under continuous illumination in an Atlas Suntest CPS+ chamber.^[27,43] Such measurements were made on non-SA and SA MAPbI₃ devices, both with and without the PVP interlayer. Metrics for all devices studied are presented in Figure 4 and in Table 2, with SPO measurements for devices shown in Figure S4.

In Figure 4a, we present device metrics for non-SA devices. We find that non-SA PSCs that were encapsulated using PVP/epoxy have a higher PCE (12.9 ± 1.5 %) than devices that were either unencapsulated (11.6 ± 1.5 %), or encapsulated with epoxy alone (11.0 ± 0.9 %). This appears to result from a non-reversible increase in device J_{SC} from (15.9 ± 0.2) mA/cm² to (17.0 ± 0.2) mA/cm² before and after encapsulation with PVP/epoxy respectively. A similar improvement in J_{SC} is also observed upon illuminating unencapsulated PSCs with the UV curing lamp as shown in Figure S2b. Intriguingly, the J_{SC} of PVP/epoxy encapsulated devices further increases on aging to an average value of (18.0 ± 0.1) mA/cm². This is accompanied by an increase in average V_{OC} from (1.05 ± 0.01) V to (1.1 ± 0.01) V. We suspect these increases in J_{SC} and V_{OC} may originate from reduced recombination at the perovskite / transport layer interfaces. This is likely due to illumination causing a photo-generated electric field which drives ion migration, with such ions reducing the density of trap-state and recombination-rates at the transport layer interfaces.^[44,45] In supplementary Figure S5(a) we plot the EQE of PSCs before and after aging where it can be seen that the integrated J_{SC} increases from 17.66 to 19.78 mA/cm². Figure S5(a-c) also demonstrates that changes in J_{SC} upon aging do not result from: (i) changes in the energetic-location of the perovskite band-edge, or (ii) changes in the morphology and distribution of grain-sizes.

In devices that were encapsulated using just epoxy, we observe a decrease in average PCE from (11.0 ± 0.1)% to (8.7 ± 0.4)% after aging, with this loss in efficiency occurring due to a reduction in FF, although this is also accompanied by an increase in J_{SC} . It appears therefore that even though the active area of the PSC is largely protected by a silver electrode, this is not sufficient to prevent device degradation – a process manifested by a ‘flick’ in the J - V sweep above V_{OC} , (see Figure 4d). This observation is generally indicative of inefficient charge extraction at one of the interfaces (most likely the top MAPbI₃-PC₆₀BM interface). It is possible that the degradation of MAPbI₃ – even in regions away from the cell area – has a negative impact on the stability of device pixels that are largely protected by the silver contact. Devices that were encapsulated by PVP/epoxy appear significantly more stable, with the PSC demonstrating no statistically-significant change in efficiency over the testing period. Such results highlight the ability of the PVP interlayer to protect the

active device layers from the epoxy and thereby resulting in enhanced PSC stability.

In Figure 4b we present device metrics for devices that were solvent annealed. Such devices start with an initially higher PCE and J_{SC} and are also characterised by a narrower distribution of device metrics. Again, no hysteresis is observable in the JV scans (see Figure 4e,f) and we find that there is no significant change in device performance upon encapsulation (even without the PVP interlayer). However, it appears that all SA devices degrade rapidly, and undergo a reduction in all performance metrics (most notably losing shunt resistance). Our measurements on non-SA PSCs described above indicate that the PVP/epoxy encapsulation is highly robust, and thus extrinsic (moisture and oxygen induced) degradation pathways in SA devices can most likely be excluded. We conclude therefore that the observed instability in encapsulated SA PSCs most likely has an intrinsic origin.

In Figure 5, we plot device metrics for SA and non-SA devices during aging over a period of up to 220 hours. The PCE of non-SA devices that were unencapsulated is presented in Figure 5a. Here, it can be seen that such devices undergo complete degradation within around 2 hours. We expect this process results from the use of a silver electrode, which has been reported to react with MAPbI_3 decomposition products (methylammonium iodide (MAI), hydriodic acid (HI) or iodide (I^-))^[46-48]. Such degradation products initially originate from exposed perovskite grain boundaries as a result of reactions involving moisture and oxygen,^[48] and then diffuse through pinholes, along grain boundaries and through the PC_{60}BM . Whilst ion migration may initially be beneficial for device performance, the device performance decreases when a significant accumulation of ions and degradation components occurs at the silver electrode. Cross-sectional SEM images of SA PSCs without encapsulation were used to better understand degradation (see Figure 2c-e). It can be seen that on aging, we evidence the presence of localised dendrite-like structures on the silver electrode surface which EDX measurements indicate contain an excess of silver and halide compared to regions of the PSC that are less degraded (Figure S6); a finding consistent with previous reports.^[44,47,49]

Figure 5b plots the time dependent PCE of non-SA PSCs that were encapsulated using just PVP. It can be seen that devices are characterised by a significant improvement in stability, with 50% of devices maintaining their initial PCE after 100 hours. The remaining devices, (data plotted using dotted lines), undergo a rapid decline in efficiency and fail after around 100 hours of operation. This indicates that despite PVP being soluble in many polar materials^[51-53], it provides some protection from oxygen and moisture ingress. Given the fact that PVP is hydrophilic and has a high WVTR ($>2000 \text{ g/m}^2\text{day}$ when used in hydrogels),^[53] we conclude that the protection it provides may result from it preferentially absorbing moisture that would otherwise migrate into the device. However without additional epoxy/glass encapsulation, it is apparent that PVP alone does not act as an effective moisture barrier-layer. For SA PSCs that were only encapsulated using PVP (see 4c), we find that all

devices fail after around 12 hours.

Figures 5d,f and 4e,g compares the stability of non-SA and SA PSCs that were encapsulated with epoxy and PVP/epoxy respectively. We find that the yield and reproducibility of devices encapsulated using PVP/epoxy is improved compared to devices encapsulated using epoxy alone. For example, from a total of 8 SA and 8 non-SA PVP/epoxy encapsulated cells, we find that only one device fails out of each device set over the 220 hour testing window. The evolution of average device metrics for non-SA and SA devices encapsulated using PVP/epoxy is shown in Figure 5h,i respectively. For non-SA devices, there is clear positive burn-in of J_{SC} that occurs over the first 30 hours of aging, however this is accompanied by a reduction in FF that results in no change in PCE during this time. Notably the PVP/epoxy encapsulation does not prevent SA devices experiencing a significant negative burn of around 40% over the first 10 hours of testing.

We have performed an extensive analysis of the lifetime of SA and non-SA devices as shown in Figure 6a. Here, we plot a histogram of extrapolated T80 lifetimes for 45 SA and 82 non-SA PSCs, with devices fabricated over a series of independent device runs. It can be seen that no SA device has a T80 above 200 hours, while a number of non-SA devices have an (extrapolated) T80 lifetime of over 2000 hours.

It is interesting to speculate on the origin of the more rapid degradation of SA PSCs. One possible explanation comes from the presence of residual DMF solvent within the perovskite that remains from the solvent annealing treatment. Studies on perovskites cast from a DMF precursor solvent suggest that residual DMF can be difficult to remove as a result of its high boiling point (153°C).^[54] To explore whether residual solvent is left in the perovskite films, we have used Fourier transform infrared spectroscopy measurements to study the non-SA and SA perovskite films (as shown in Figure S7), however we failed to detect even trace amounts of DMF in such films. We note that recent work has demonstrated a differential degradation of individual (and even adjacent) perovskite grains. Indeed, grains with different defect densities or stoichiometry can result in some grains being more stable than others.^[55] It can be seen in the SEM cross-section image of a SA-device shown in Figure 2d that some grains are dark and completely degraded whilst others likely remain as MAPbI₃ even after aging. We have also found (see Figure S6) that there is also a large variation in the quality and uniformity of the silver contact after aging. We speculate that the quasi-stable liquid-phase environment established during solvent annealing increases the mobility of ions such that the larger resultant grains have a wider distribution of stoichiometric and ionic defects relative to a non-SA MAPbI₃ film. This inhomogeneity will likely lead to an increased tendency for instability, particularly in grains having a PbI₂ deficit.^[55] It is also possible that the increased roughness of the SA MAPbI₃ relative to non-SA MAPbI₃ (from 6.5nm to 19nm - see Figure 2a,b and S2) might result in reduced device stability. Here, increased roughness of the interface between the MAPbI₃ and the PC₆₀BM may

facilitate the diffusion of MAI, HI and I⁻ into the PC₆₀BM and then to the silver top contact, resulting in enhanced device degradation.

Our previous study on the stability of PSC devices incorporating a PEDOT:PSS hole-extraction layer demonstrated that device lifetime was limited to ~300 hours. Here, we ascribed this instability to the presence of moisture trapped within the hygroscopic and acidic PEDOT:PSS.^[27,29,56] The PVP/epoxy system developed here allows us to test this hypothesis, and we therefore explored replacing the poly-TPD HTM with PEDOT:PSS. The enhanced hydrophilic nature of PEDOT:PSS can be evidenced from contact-angle measurements, with relative contact angles for PEDOT:PSS and poly-TPD being $15.1 \pm 2.1^\circ$ and $60.2 \pm 4.1^\circ$ respectively (see Figure S8). We find such devices incorporating PEDOT:PSS undergo a rapid reduction in device metrics, with devices completely failing after 24 hours (see Figure S9). This result highlights a clear correlation between the use of hydrophobic charge extraction layers and long term operational stability in PSCs.

Finally, using our encapsulation system we can explore the stability of non-SA MAPbI₃ devices over an extended time-period. This is shown in Figure 6b, where we follow the efficiency of a device encapsulated with epoxy/PVP over a period of 1500 hours. It can be seen that after 1000 hours of testing, the device retained 80% of its starting efficiency; a result that was expected given the expected extrapolated T80 lifetimes in Figure 6a. After this long burn, the device efficiency stabilised, indicating that its T80 lifetime after burn-in is likely to be in the range of 1000s of hours. Note that the device was periodically removed from the aging setup to record calibrated AM1.5G *J-V* measurements as shown in Figure 6c. This confirmed that device PCE had dropped from 13.2% to 11.9% after 1500 hours of aging, corresponding to a burn-in of 15%. These values were obtained from both *J-V* sweeps as well as SPO measurements (see Figure 6d) that were recorded at the same time (see data summary presented in Table 2).

In summary, we have demonstrated that PVP not only acts as a protective interlayer to protect MAPbI₃ based solar cells from the epoxy used to encapsulate such devices, but is also able to provide partial protection from moisture and oxygen. By combining PVP, epoxy and glass we develop a highly effective multi-layer encapsulation system, achieving T80 lifetimes of 1000 hours for inverted architecture MAPbI₃ PSCs. We expect that such a solution-processable interlayer system could be integrated into a cheap roll-to-roll process suitable for manufacture. We highlight the importance of isolating PSCs from the damaging effects of epoxy and expect there are other materials (both polymeric and dielectric) that could also be used as barrier interlayers for PSC encapsulation, provided that the deposition of such interlayers does not damage the PSC. We demonstrate that these impressive lifetimes for inverted architecture PSCs are reliant on the use of a hydrophobic polymer hole transport material, poly-TPD, instead of the more commonly utilized hydrophilic PEDOT:PSS. We use this encapsulation system to explore the comparative stability of PSCs containing a MAPbI₃

active layer that had been initially exposed to solvent vapour (a solvent-annealing process) which we show increases the average size of the perovskite crystal grains. This annealing process results in an initial increase in device PCE, with the non solvent-annealed control and the solvent annealed device having a peak efficiency of 15.3% and 17.6% respectively. We find however that this initial efficiency gain is rapidly lost over a 10-hour burn-in period, with the efficiency of the solvent annealed device falling below that of the non-solvent annealed control. Our results indicate that more research is required to understand what steps may be required to stabilise solvent annealed PSC and that higher efficiency PSC devices do not necessarily have long-term intrinsic-stability. Optimisation of device stability should be viewed as an important separate task to the optimisation of efficiency. With encapsulation equivalent to our successful multi-layer sealing and device optimisation driven to obtain stability, MAPbI₃ based PSCs can operate effectively for thousands of hours. Combining these developments with perovskite compositional advancements paves the way for stability lasting the years needed for commercialisation.

Experimental Methods

Materials and handling: All solvents, except those used for cleaning, were purchased from Sigma Aldrich in their anhydrous form and stored in a nitrogen filled glovebox. All dry powders were stored under vacuum. Dry powders were weighed out in air, with all solvents added to the dry powders in the glovebox. All solutions were filtered with a 0.45 μ m polytetrafluoroethylene (PTFE) filter shortly before deposition with spin-coating performed in the glove-box using a dynamic technique.

Device fabrication: Perovskite Solar Cells (PSCs) were fabricated on 20 Ω / square pre-patterned ITO glass photovoltaic substrates. Substrates were first sonicated for 10 minutes in hot Hellmanex detergent solution, then placed in boiling deionised (DI) water, sonicated for 10 minutes in hot DI water, followed by a final 10 minute sonication in isopropyl alcohol (IPA). Shortly before deposition of the hole-transport layer, substrates were dried with a nitrogen gun and UV ozone cleaned for 15 minutes. Poly(N,N'-bis-4-butylphenyl-N,N'-bisphenyl)benzidine (poly-TPD) and 2,3,5,6-tetrafluoro-7,7,8,8-tetracyanoquinodimethane (F4-TCNQ) were dissolved in toluene at 1 mg/ml and 0.2 mg/ml respectively. The poly-TPD solution was heated to 80°C to fully dissolve the solution. Following Wang *et al.*^[20], the poly-TPD was spin-coated from a hot solution onto a recently UV-ozone cleaned substrate at a speed of 4000 rpm to create a uniform ultra-thin poly-TPD film. This was then annealed at 110°C for 10 minutes before being transferred to the glovebox. The methylamine bubbled acetonitrile MAPbI₃ was made following the procedure described by Noel *et al.*^[33] A 0.5M solution composed of methylammonium iodide to lead iodide (99.99%) at a ratio of 1:1.06 was then spin-coated on the poly-TPD at 4000 rpm in the glovebox.^[33] The resulting 350-400 nm thick MAPbI₃ film was then annealed at 100°C for 45 minutes in the glovebox. To solvent anneal the PSCs, the

MAPbI₃ films were held at 100°C for a further 30 minutes. During the first 15 minutes of this anneal, they were sealed under a glass petri dish in a solvent atmosphere created using 20 μl of dimethylformamide (DMF). After 15 minutes, the petri-dish lid was then removed. After the ITO/poly-TPD/MAPbI₃ films had cooled to room temperature a 30 mg/ml [6,6]-phenyl-C61-butyric acid methyl ester (PC₆₀BM) solution in chlorobenzene (which had been stirred overnight at 70°C and then left to cool before deposition) was spin-coated at 3000 rpm to produce a 100 nm thick PC₆₀BM layer. The substrates were annealed again for 10 minutes at 90°C in a glovebox. After the ITO/poly-TPD/MAPbI₃/PC₆₀BM films had cooled to room temperature an ultra-thin bathophenanthroline (Bphen) layer was spin-coated from a 0.5 mg/ml IPA solution at 6000 rpm in a glovebox. Before completing the PSCs the entire ITO/poly-TPD/MAPbI₃/PC₆₀BM/BPhen stack was brought into a humidity controlled clean room (<35% RH) and held at 80°C whilst being patterned with a DMF coated cotton bud to swab the sides and edges of the substrate (see an image of the swabbed films in Figure 1a:v). After cooling and returning to the glovebox, the patterned substrates were placed in a thermal evaporator and left overnight under a < 2x10⁻⁶ pa vacuum. The following day a 100 nm Ag cathode was thermally evaporated onto the film surface at a rate of 1 Ås⁻¹. The final device layout for an encapsulated PSC is shown in Figure 1b. Here we show a completed PSC device has 8 cells formed by the overlap between Ag cathodes and ITO anode, with each cell having an active area of 0.04 cm². The PSCs were taken back into the glovebox and either left without encapsulation, or coated with 135 ± 5 nm of polyvinylpyrrolidone (Sigma Aldrich) spin-coated at 6000 rpm from a 25 mg/ml methanol solution, or coated with a drop of UV initiated one part epoxy (Ossila), covered with a glass encapsulation slide and cured under a UV light for 20 minutes, or encapsulated with both PVP and epoxy. The encapsulation materials were deposited to cover the whole PSC stack. Note that the glass slide can usually only be removed with force (a process that which often also results in the removal of other PSC layers), indicating that the epoxy makes a strong seal to the PSC, even in the presence of a PVP interlayer. All layer thicknesses reported here and shown in Figure 1b were measured using a Bruker DektakXT profilometer and confirmed with cross-sectional SEM as detailed below.

Device characterisation: Device performance was determined under ambient conditions by measuring *J-V* curves using a Newport 92251A-1000 solar simulator, with devices illuminated through a 0.0256 cm² aperture mask. Before each set of measurements, the intensity was calibrated to 100 mWcm⁻² using an NREL certified silicon reference cell. The applied bias was swept from 0.0 V to +1.2 V and back again at a scan speed of 0.4 Vs⁻¹ using a Keithley 237 source measure unit. The *V_{mpp}* of each device was extracted from the *J-V* scans, and the stabilised power output was recorded by holding the devices at their *V_{mpp}*.

Lifetime testing: Device aging was completed using an Atlas Suntest CPS+ with a 1500W Xenon bulb, quartz IR reducing filters and internal reflectors. We have previously shown that the

lamp spectrum approximately matches AM1.5G^[27,43]. The Xenon bulb in combination with internal reflectors produce an irradiance level of ~ 100 mW/cm². This bulb was replaced several times during the longest lifetime-testing experiments. All lifetime PCE and J_{SC} measurements reported here are normalised to 7 silicon photodiodes that take into account fluctuations in the illumination intensity. Device performance was determined from reverse sweep J - V measurements. Here, the applied bias was swept from 1.15 V to 0 V at a scan speed of 0.05 Vs⁻¹ using a Keithley 2400 source measure unit. Devices were not swept into negative voltage as we have found this reduces device stability, and were held at open circuit between measurements, with every device being scanned every 15 minutes. The temperature of the PSCs inside the Suntest was (42 \pm 3) °C during operation. The humidity was not controlled, but was found to be within the range (38 \pm 6)% RH over the entire course of the exposure. PSCs mounted in the Suntest were not covered by an aperture mask during lifetime testing, and thus device metrics are normalised to their initial values. T80 lifetimes were extracted directly when possible or extrapolated using a linear fit applied to the post burn-in region.

Absorbance: UV-vis absorption measurements were performed under ambient conditions using a UV-VIS-NIR light source (Ocean Optics – DH-2000-BAL), and spectrometer (Ocean Optics – HR2000+ES). All data reported here is presented as absorbance. Samples for absorption measurements were prepared on quartz-coated glass, using the same deposition methods as used in device fabrication. All absorbance measurements of films that have been encapsulated have had the absorbance of the reference encapsulation system subtracted.

Contact angle: A contact angle goniometer (Ossila) was used to determine the sessile contact angle from images of droplets of deionized water on poly-TPD and PEDOT:PSS.

Scanning electron microscopy (SEM) & energy dispersive x-ray spectroscopy (EDX): An Inspect F, FEI Helios NanoLab G3 UC and Nova Nano 450 were used to image the surfaces of MAPbI₃ (at 2keV) and cross-section of PSCs device stacks (at 1keV). For top view samples, MAPbI₃ was deposited on ITO/poly-TPD substrates. Further details of the mounting of samples and use of the SEM are given in our previous work.^[17] Compositional analysis was performed using energy dispersive X-ray spectroscopy (EDX-SEM) using the Helios NanoLab at 10 keV accelerating voltage, with the signal measured using an Oxford Instruments EDX spectrometer and analysed using AZtecEnergy spectral analysis software.

Atomic force microscopy: A Veeco Dimension 3100 with a nanoscope IIIA controller operated in tapping mode was used to characterise the surface topography of the non-solvent annealed and solvent annealed samples.

Fourier transform infrared spectroscopy (FTIR): To explore whether residual solvent remained in the MAPbI₃ films, they were deposited on quartz glass and annealed for 60 minutes. They

were then solvent annealed for 5 minutes with solvent volume increased to 100 μ l. No subsequent annealing was applied in order to maximise the quantity of any residual solvent. Films were then removed from the substrate using a razor blade, with the resultant powder investigated using a PerkinElmer 100 attenuated total reflection-IR (ATR-IR) spectrometer.

External Quantum Efficiency (EQE): External quantum efficiencies were measured using a white light source that was monochromated using a Spectral Products DK240 monochromator that was then imaged on the PSC active-area. The intensity of the monochromated light was determined using a calibrated silicon photodiode having a known spectral response. The external quantum efficiency was measured across two scanning ranges (380 - 700 nm and 600-850 nm) using an Xtralien X100 (Ossila) source measure unit to determine the PSC photocurrent.

Supporting Information: Supporting Information is available online.

Acknowledgements This work was funded by the UK Engineering and Physical Sciences Research Council (EPSRC) via grants EP/M025020/1 ‘High resolution mapping of performance and degradation mechanisms in printable photovoltaic devices’, EPSRC grant EP/N008065/1 ‘Secondary Electron Emission - Microscopy for Organics With Reliable Engineering-Properties’, and EP/M014797/1 ‘Improved Understanding, Development and Optimization of Perovskite-based Solar Cells’. We also thank the EPSRC for PhD studentships via the University of Sheffield DTG account (T.R.) and from the Centre for Doctoral Training in New and Sustainable PV, EP/L01551X/1 (M.S., B.F., J.S.). We also would like to thank Dr James Kingsley, Dr Nick Scarratt, Claire Greenland, Emma Spooner, and Rachel Kilbride for useful discussions.

Received: ((will be filled in by the editorial staff))

Revised: ((will be filled in by the editorial staff))

Published online: ((will be filled in by the editorial staff))

References

- [1] W. S. Yang, B.-W. Park, E. H. Jung, N. J. Jeon, Y. C. Kim, D. U. Lee, S. S. Shin, J. Seo, E. K. Kim, J. H. Noh, S. Il Seok, *Science* **2017**, 356, 1376.

- [2] M. Stolterfoht, C. M. Wolff, Y. Amir, A. Paulke, L. Perdigón-Toro, P. Caprioglio, D. Neher, *Energy Environ. Sci.* **2017**, *10*, 1530.
- [3] M. Saliba, T. Matsui, K. Domanski, J.-Y. Seo, A. Ummadisingu, S. M. Zakeeruddin, J.-P. Correa-Baena, W. R. Tress, A. Abate, A. Hagfeldt, M. Gratzel, *Science* **2016**, 5557.
- [4] M. Saliba, T. Matsui, J.-Y. Seo, K. Domanski, J.-P. Correa-Baena, M. K. Nazeeruddin, S. M. Zakeeruddin, W. Tress, A. Abate, A. Hagfeldt, M. Grätzel, *Energy Environ. Sci.* **2016**, *9*, 1989
- [5] M. Abdi-Jalebi, Z. Andaji-Garmaroudi, S. Cacovich, C. Stavrakas, B. Philippe, J. M. Richter, M. Alsari, E. P. Booker, E. M. Hutter, A. J. Pearson, S. Lilliu, T. J. Savenije, H. Rensmo, G. Divitini, C. Ducati, R. H. Friend, S. D. Stranks, *Nature* **2018**, 555, 497.
- [6] T. Bu, X. Liu, Y. Zhou, J. Yi, X. Huang, L. Luo, J. Xiao, Z. Ku, Y. Peng, F. Huang, Y.-B. Cheng, J. Zhong, *Energy Environ. Sci.* **2017**, *10*, 2509.
- [7] NREL Efficiency Chart, March **2018**.
- [8] D.-Y. Son, S.-G. Kim, J.-Y. Seo, S.-H. Lee, H. Shin, D. Lee, N.-G. Park, *J. Am. Chem. Soc.* **2018**, *140*, 1358.
- [9] E. T. Hoke, D. J. Slotcavage, E. R. Dohner, A. R. Bowring, H. I. Karunadasa, M. D. McGehee, *Chem. Sci.* **2014**, *0*, 1.
- [10] J. A. Christians, P. Schulz, J. S. Tinkham, T. H. Schloemer, S. P. Harvey, B. J. T. de Villers, A. Sellinger, J. J. Berry, J. M. Luther, *Nat. Energy* **2018**, *3*.
- [11] Z. H. Bakr, Q. Wali, A. Fakharuddin, L. Schmidt-Mende, T. M. Brown, R. Jose, *Nano Energy* **2017**, *34*, 271.
- [12] S. N. Habisreutinger, B. Wenger, H. J. Snaith, R. J. Nicholas, *ACS Energy Lett.* **2017**, *2*, 622.
- [13] F. Wang, M. Endo, S. Mouri, Y. Miyauchi, Y. Ohno, A. Wakamiya, Y. Murata, K. Matsuda, *Nanoscale* **2016**, *8*, 11882.
- [14] L. Calió, S. Kazim, M. Grätzel, S. Ahmad, *Angew. Chemie Int. Ed.* **2016**, *2*.
- [15] Q. Wang, C. Bi, J. Huang, *Nano Energy* **2015**, *15*, 275.
- [16] D. Zhao, M. Sexton, H. Y. Park, G. Baure, J. C. Nino, F. So, *Adv. Energy Mater.* **2015**, *5*, 1401855.
- [17] M. Wong-Stringer, J. E. Bishop, J. A. Smith, D. K. Mohamad, A. J. Parnell, V. Kumar, C. Rodenburg, D. G. Lidzey, *J. Mater. Chem. A* **2017**, *5*, 15714.
- [18] Q. Liu, M. C. Qin, W. J. Ke, X. L. Zheng, Z. Chen, P. L. Qin, L. Bin Xiong, H. W. Lei, J. W. Wan, J. Wen, G. Yang, J. J. Ma, Z. Y. Zhang, G. J. Fang, *Adv. Funct. Mater.* **2016**, *26*, 6069.
- [19] B. Roose, J. P. C. Baena, K. C. Gödel, M. Graetzel, A. Hagfeldt, U. Steiner, A. Abate, *Nano Energy* **2016**, *30*, 517.

- [20] J. T.-W. Wang, Z. Wang, S. K. Pathak, W. Zhang, D. deQuilettes, F. Wisnivesky, J. Huang, P. Nayak, J. Patel, Hanis Yusof, Y. Vaynzof, R. Zhu, I. Ramirez, J. Zhang, C. Ducati, C. Grovenor, M. Johnston, D. S. Ginger, R. Nicholas, H. Snaith, *Energy Environ. Sci.* **2016**, *9*, 2892.
- [21] J. Kim, M. A. M. Teridi, A. R. bin M. Yusoff, J. Jang, W. S. Yang, G. Niu, X. Guo, L. Wang, C.-G. Wu, J. H. Heo, M. Jørgensen, K. Norrman, F. C. Krebs, L. S. C. Pingree, B. A. MacLeod, D. S. Ginger, Z. Wu, J. T.-W. Wang, H. Choi, M. Liu, M. B. Johnston, H. J. Snaith, P.-W. Liang, N. J. Jeon, H.-B. Kim, H. J. Snaith, M. R. Filip, G. E. Eperon, H. J. Snaith, F. Giustino, *Sci. Rep.* **2016**, *6*, 1234.
- [22] L. Yang, A. T. Barrows, D. G. Lidzey, T. Wang, *Reports Prog. Phys.* **2016**, *79*, 026501.
- [23] H. J. Snaith, *J. Phys. Chem. Lett* **2013**, *4*, 3623.
- [24] Z. Zhou, S. Pang, Z. Liu, H. Xu, G. Cui, *J. Mater. Chem. A* **2015**, *3*, 19205.
- [25] R. Cheacharoen, N. J. Rolston, D. Harwood, K. A. Bush, R. H. Dauskardt, M. D. McGehee, *Energy Environ. Sci.* **2017**, *11*, 144.
- [26] Y. Zhang, H. Yi, A. Iraqi, J. Kingsley, A. Buckley, T. Wang, D. G. Lidzey, *Sci. Rep.* **2017**, *7*, 1.
- [27] C. Bracher, B. G. Freestone, D. K. Mohamad, J. A. Smith, D. G. Lidzey, *Energy Sci. Eng.* **2017**, *6*, 35
- [28] Y. Zhang, E. Bovill, J. Kingsley, A. R. Buckley, H. Yi, A. Iraqi, T. Wang, D. G. Lidzey, *Sci. Rep.* **2016**, *6*, 21632.
- [29] W. Lee, M. Song, S. Park, S. Nam, J. Seo, H. Kim, Y. Kim, *Sci. Rep.* **2016**, *6*, 1.
- [30] L. Shi, T. L. Young, J. Kim, Y. Sheng, L. Wang, Y. Chen, Z. Feng, M. J. Keevers, X. Hao, P. J. Verlinden, M. A. Green, A. W. Y. Ho-Baillie, *ACS Appl. Mater. Interfaces* **2017**, *9*, 25073.
- [31] F. Matteocci, L. Cinà, E. Lamanna, S. Cacovich, G. Divitini, P. A. Midgley, C. Ducati, A. Di Carlo, *Nano Energy* **2016**, *30*, 162.
- [32] Q. Dong, F. Liu, M. K. Wong, H. W. Tam, A. B. Djurišić, A. Ng, C. Surya, W. K. Chan, A. M. C. Ng, *ChemSusChem* **2016**, *9*, 2518.
- [33] N. K. Noel, S. N. Habisreutinger, B. Wenger, M. T. Klug, M. T. Hörantner, M. B. Johnston, R. J. Nicholas, D. T. Moore, H. Snaith, *Energy Environ. Sci.* **2017**, *10*, 145.
- [34] X. Xu, C. Ma, Y. Cheng, Y. M. Xie, X. Yi, B. Gautam, S. Chen, H. W. Li, C. S. Lee, F. So, S. W. Tsang, *J. Power Sources* **2017**, *360*, 157.
- [35] X. Zheng, B. Chen, J. Dai, Y. Fang, Y. Bai, Y. Lin, H. Wei, X. C. Zeng, J. Huang, *Nat. Energy* **2017**, *2*, 17102.
- [36] N. Tripathi, Y. Shirai, M. Yanagida, A. Karen, K. Miyano, *ACS Appl. Mater. Interfaces* **2016**, *8*, 4644.
- [37] J. Lee, H. Kang, G. Kim, H. Back, J. Kim, S. Hong, B. Park, E. Lee, K. Lee, *Adv. Mater.* **2017**, *29*, 1.
- [38] J. Liu, C. Gao, X. He, Q. Ye, L. Ouyang, D. Zhuang, C. Liao, J. Mei, W. Lau, *ACS Appl. Mater.*

- Interfaces* **2015**, 7, 24008.
- [39] Y. Zhou, O. S. Game, S. Pang, N. P. Padture, *J. Phys. Chem. Lett.* **2015**, 6, 4827.
- [40] Y. Wang, S. Li, P. Zhang, D. Liu, X. Gu, H. Sarvari, Z. Ye, J. Wu, Z. Wang, Z. D. Chen, *Nanoscale* **2016**, 8, 19654.
- [41] Z. Xiao, Q. Dong, C. Bi, Y. Shao, Y. Yuan, J. Huang, *Adv. Mater.* **2014**, 26, 6503.
- [42] L. Shi, T. L. Young, J. Kim, Y. Sheng, L. Wang, Y. Chen, Z. Feng, M. J. Keevers, X. Hao, P. J. Verlinden, M. A. Green, A. W. Y. Ho-Baillie, *ACS Appl. Mater. Interfaces* **2017**, 9, 25073.
- [43] E. Bovill, N. Scarratt, J. Griffin, H. Yi, A. Iraqi, A. R. Buckley, J. W. Kingsley, D. G. Lidzey, *Appl. Phys. Lett.* **2015**, 106, 073301.
- [44] P. Calado, A. M. Telford, D. Bryant, X. Li, J. Nelson, B. C. O'Regan and P. R. F. Barnes, *Nat. Commun.*, 2016, 7, 13831.
- [45] T. Zhang, S. H. Cheung, X. Meng, L. Zhu, Y. Bai, C. H. Y. Ho, S. Xiao, Q. Xue, S. K. So, S. Yang, *J. Phys. Chem. Lett.* 2017, 8, 5069.
- [46] J. Li, Q. Dong, N. Li, L. Wang, *Adv. Energy Mater.* **2017**, 7, 1.
- [47] Y. Kato, L. K. Ono, M. V. Lee, S. Wang, S. R. Raga, Y. Qi, *Adv. Mater. Interfaces* **2015**, 2, 2.
- [48] Y. Han, S. Meyer, Y. Dkhissi, K. Weber, J. M. Pringle, U. Bach, L. Spiccia, Y.-B. Cheng, *J. Mater. Chem. A* **2015**, 3, 8139.
- [49] Q. Sun, P. Fassel, D. Becker-Koch, A. Bausch, B. Rivkin, S. Bai, P. E. Hopkinson, H. J. Snaith, Y. Vaynzof, *Adv. Energy Mater.* **2017**, 7, 170097.
- [50] Y. Kato, L. K. Ono, M. V Lee, S. Wang, S. R. Raga, Y. Qi, *Adv. Mater. Interfaces* **2015**, 2, 1500195.
- [51] K. Nasouri, A. M. Shoushtari, M. R. M. Mojtahedi, *Adv. Polym. Technol.* **2015**, 34, 1.
- [52] M. Teodorescu, M. Bercea, *Polym. - Plast. Technol. Eng.* **2015**, 54, 923.
- [53] A. Zheng, Y. Xue, D. Wei, S. Li, H. Xiao, Y. Guan, *Soft Mater.* **2014**, 12, 297.
- [54] A. E. Williams, P. J. Holliman, M. J. Carnie, M. L. Davies, D. a. Worsley, T. M. Watson, *J. Mater. Chem. A* **2014**, 2, 19338.
- [55] J. Barbé, V. Kumar, M. J. Newman, H. K. H. Lee, S. M. Jain, H. Chen, C. Charbonneau, C. Rodenburg, W. C. Tsoi, *Sustain. Energy Fuels* **2018**, 2, 905.
- [56] A. J. Parnell, A. J. Cadby, A. D. F. Dunbar, G. L. Roberts, A. Plumridge, R. M. Dalglish, M. W. A. Skoda, R. A. L. Jones, *J. Polym. Sci. Part B Polym. Phys.* **2016**, 54, 141.

Figures

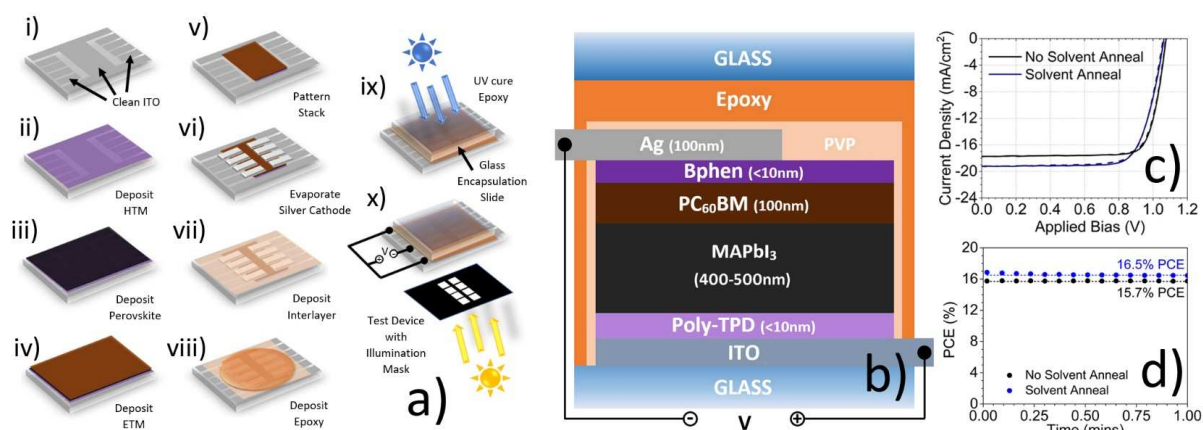


Figure 1: (a) A schematic of the fabrication and testing routine used to create perovskite solar cells incorporating a PVP/epoxy encapsulation. (b) Device architecture showing all layers, together with their approximate thicknesses. (c) Current-voltage sweeps and (d) stabilised power outputs for champion devices with the thermally annealed MAPbI₃ active layer (black) and with additional solvent annealing (blue). Dashed and solid lines represent forward and reverse sweep directions respectively.

	Solvent Anneal	No Solvent Anneal
PCE [%] (<i>Stabilised</i>)	17.55 (16.5)	15.31 (15.7)
J_{sc} [mA/cm ²]	20.21	17.77
V_{oc} [V]	1.08	1.08
FF [%]	79.81	80.12

Table 1: Solar cell performance parameters for champion devices either with or without solvent annealing.

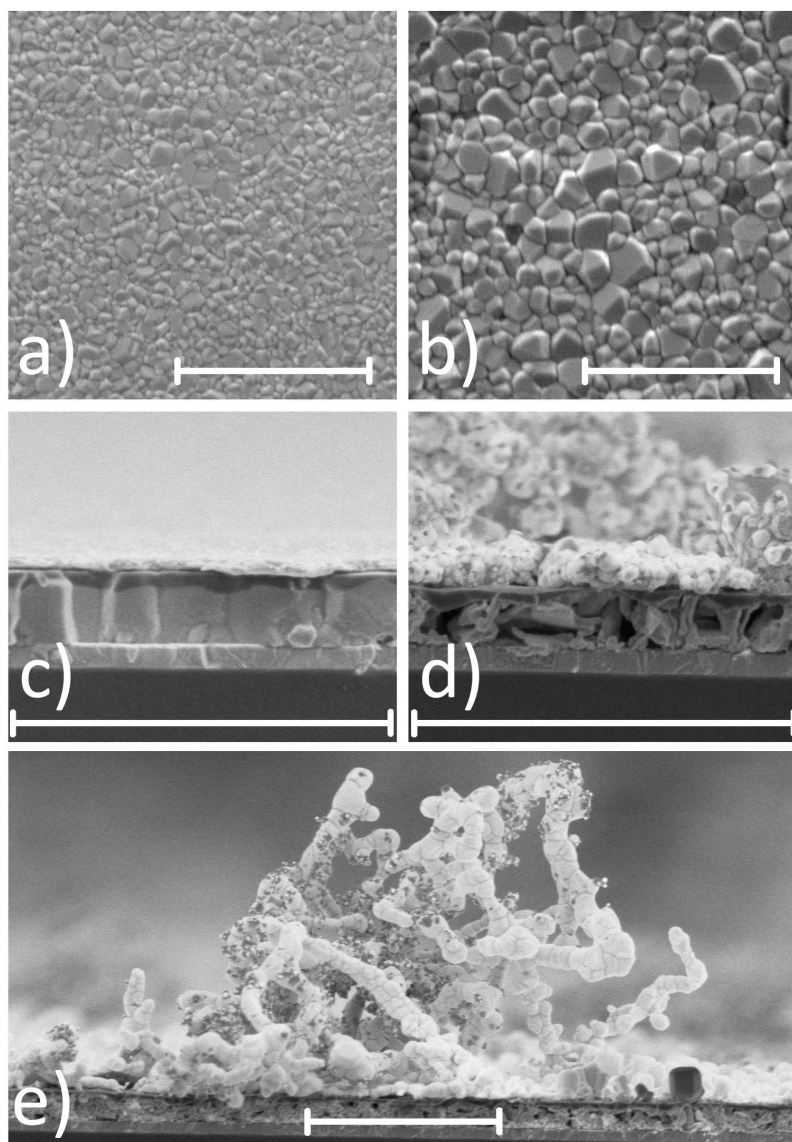


Figure 2:

Parts (a) and (b) show a top view scanning electron microscopy (SEM) images of MAPbI₃ prior to solvent annealing in (a), and after solvent annealing in (b). Parts (c) and (d) show cross-sectional SEM images: fresh solvent annealed device in (c), and a solvent annealed device aged without encapsulation in (d). The growth of silver iodide dendrites on another degraded device (as confirmed in Figure S6) can be clearly seen in part (e). All scale bars are 2 μm.

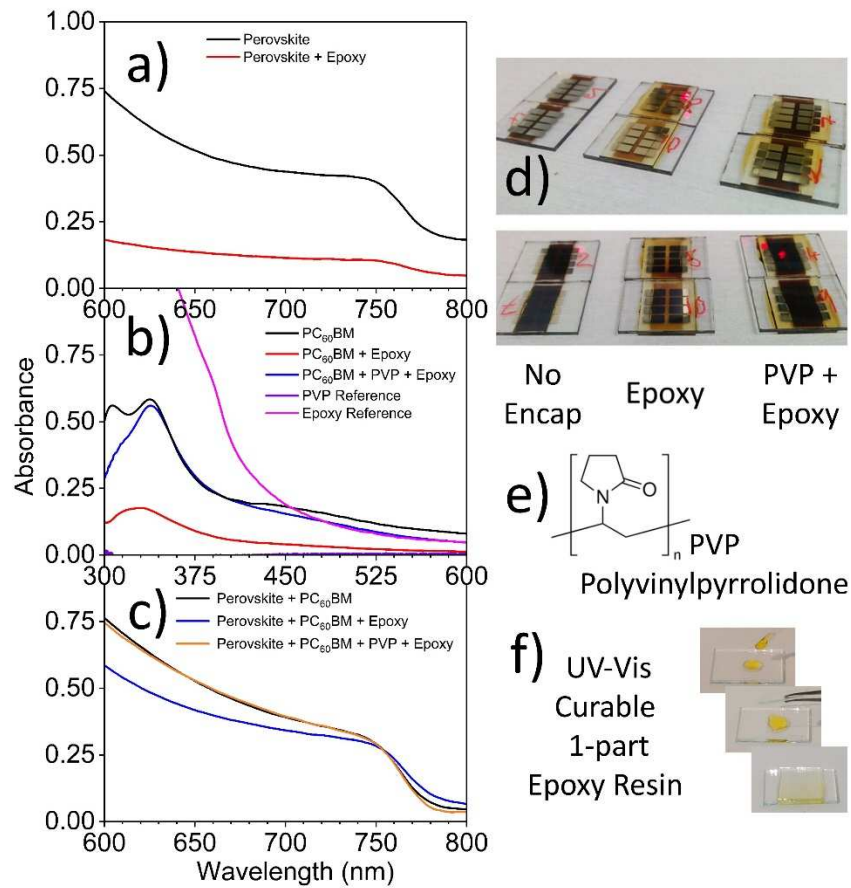


Figure 3: Absorbance spectra of various material combinations. Part (a) shows absorbance spectra recorded for MAPbI₃ (black) and epoxy encapsulated MAPbI₃ (red). (b) Absorbance spectra for pure PC₆₀BM (black), and PC₆₀BM after encapsulation with epoxy (red) and with a PVP interlayer placed between PC₆₀BM and epoxy (PVP/epoxy encapsulated, blue). Reference absorbance spectra of epoxy (pink) and PVP (purple) are also shown (note that PVP has negligible absorbance across all observed wavelengths). (c) Absorbance spectra of MAPbI₃/PC₆₀BM before (black) and after encapsulation with epoxy (blue) and with PVP/epoxy (orange). (d) Photographs of completed devices using different encapsulation routines, (e) the chemical structure of PVP and (f) the epoxy deposition process.

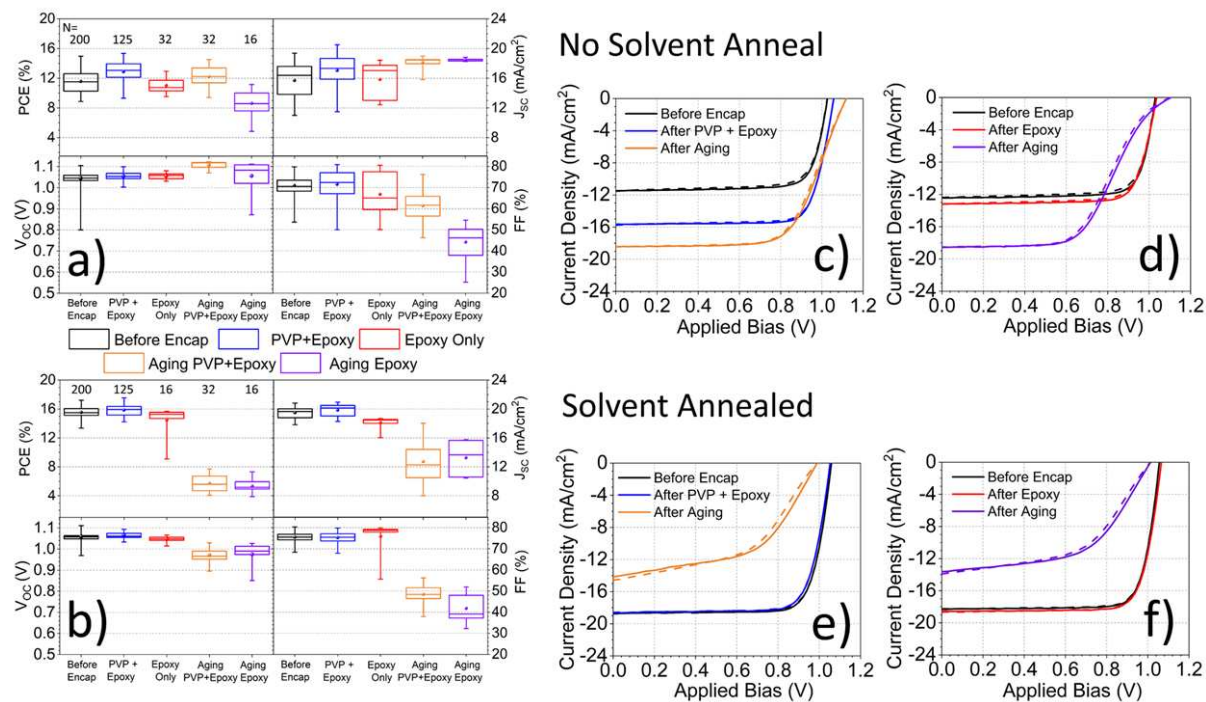


Figure 4: Parts (a) and (b) present box plots of all performance metrics from both forward and reverse sweeps for PSCs. Specifically, part (a) shows data for PSCs without solvent annealing, and part (b) shows data for solvent annealed devices. In both cases, data is presented at various stages of encapsulation and after 200 hours aging under 1 sun illumination. Data recorded before encapsulation is shown using black symbols, after encapsulation with epoxy only (red symbols), epoxy-only after aging (purple), with a PVP interlayer and epoxy (blue) and PVP/epoxy after aging (orange). The number of cell measurements recorded for each condition are presented in the PCE plot in parts (a) and (b). Extreme outliers, such as cells that have fully degraded due to encapsulation failure are not included. Representative J - V sweeps before and after encapsulation and subsequent aging are presented in parts (c) to (f). Specifically, devices in which no solvent anneal was used are summarised in parts (c) and (d), with solvent annealed devices in (e) and (f). In all cases, we show data for devices that were either encapsulated with epoxy only, or with epoxy and PVP.

	PVP + Epoxy			Epoxy		
	Before Encapsulation	After Encapsulation	After 200 Hours Aging	Before Encapsulation	After Encapsulation	After 200 Hours Aging
No Solvent Anneal						
PCE [%] (<i>Stabilised</i>)	9.21	13.14 (12.8)	13.75 (14.1)	10.11	10.63 (10.4)	11.16 (12.4)
J_{sc} [mA/cm ²]	11.48	15.62	18.46	12.45	13.19	18.53
V_{oc} [V]	1.03	1.05	1.12	1.02	1.03	1.11
FF [%]	78.16	79.94	66.66	78.87	77.84	54.51
Solvent Anneal						
PCE [%] (<i>Stabilised</i>)	15.62	15.26 (14.7)	7.4 (7.2)	15.55	15.70 (14.7)	7.32 (7.2)
J_{sc} [mA/cm ²]	18.75	18.67	14.18	18.32	18.58	13.91
V_{oc} [V]	1.05	1.05	0.99	1.06	1.07	1.01
FF [%]	78.67	77.63	52.79	80.38	79.31	51.95

Table 2: Performance metrics for representative devices. Here, data includes PVP/epoxy and epoxy-only devices that are either solvent annealed (SA) or non-solvent annealed (non-SA). We use the following colour-scheme for the text: before encapsulation (black), after encapsulation (blue and red) and after aging (orange and purple). Stabilised measurements were not performed before encapsulation to minimise device degradation.

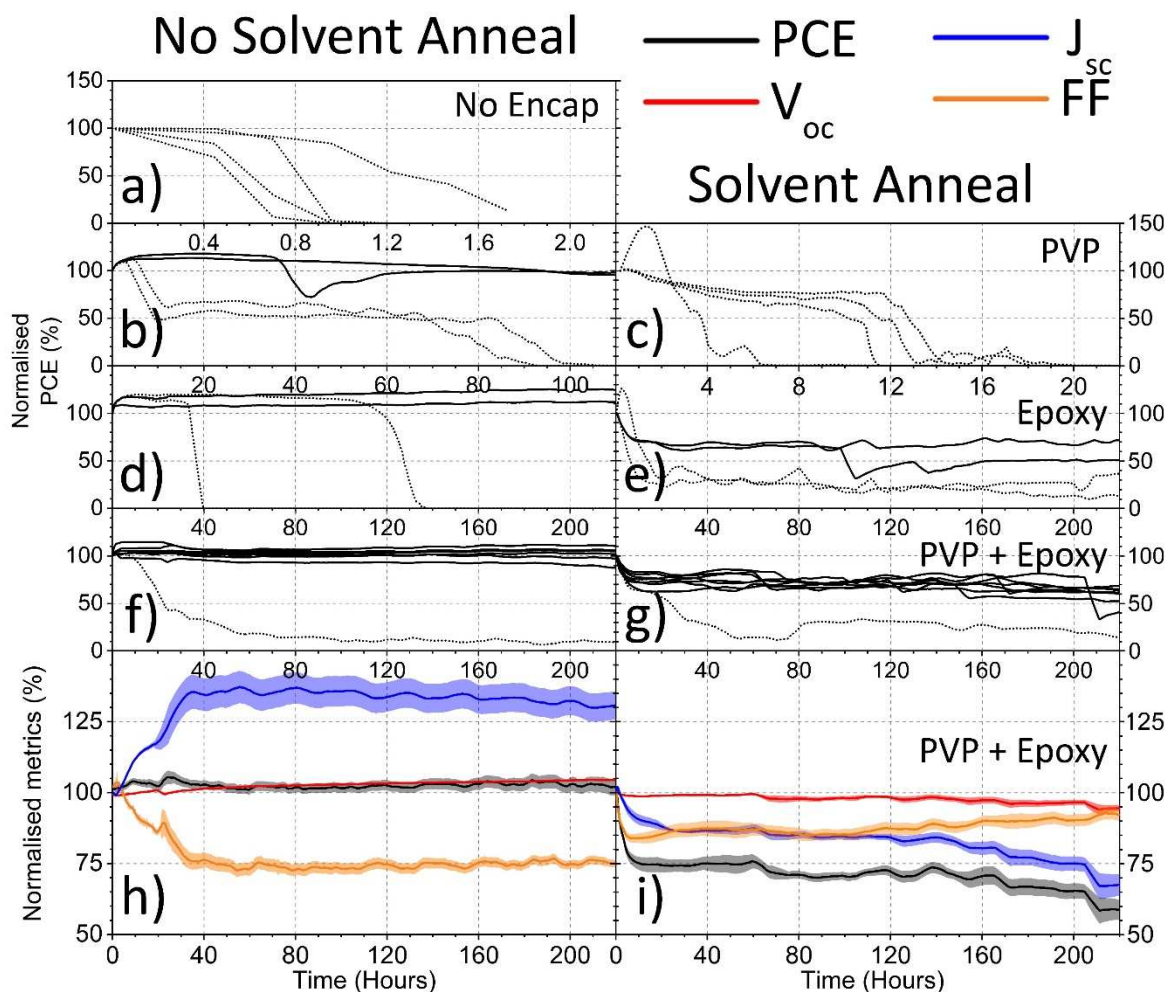


Figure 5: The effect of aging under illumination and load on device performance. The figures plot the normalised PCE (black) over time for individual cells. Here, data is split into non-solvent annealed devices (left column) and solvent annealed devices (right column). Devices are either (a) without encapsulation, (b) and (c) PVP encapsulated, (d) and (e) encapsulated with epoxy only or (f) and (g) encapsulated with PVP/epoxy. Solid lines are used to plot data for individual devices that we consider to be stable, with dotted lines indicating devices that have degraded much faster than other stable devices. For each sub-plot, we present data recorded from 4 devices, except for the plot summarising PVP/epoxy encapsulated devices, where data for 8 devices is shown. Parts (h) and (i) present normalised device metrics (J_{sc} - blue, V_{oc} - red, FF - orange) over time for PVP/epoxy encapsulated devices. Here, part (h) corresponds to devices that were not solvent annealed with part (i) corresponding to with solvent annealed devices. In all cases, the plotted line represents the mean of device measurements with the translucent band representing the standard deviation of all cells.

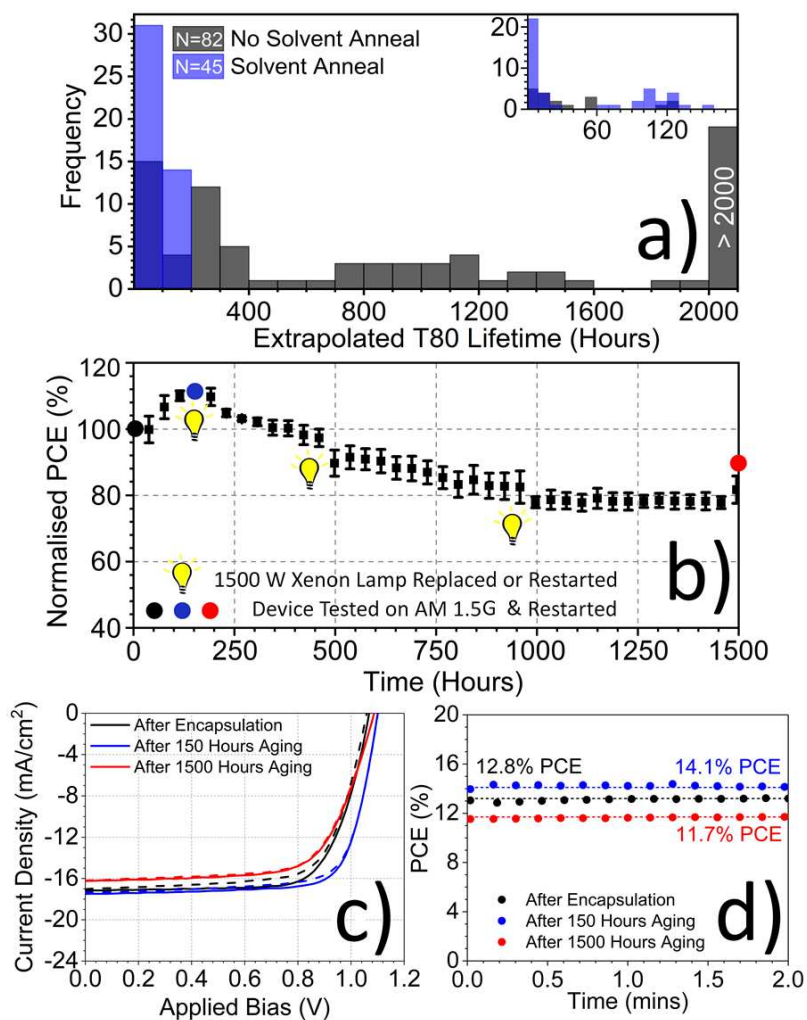


Figure 6: Part (a) shows a histogram of extrapolated PSC T80 lifetime for devices containing solvent-annealed (blue) or non-solvent annealed (black) perovskite films. The inset highlights device data recorded over the first 200 hours of measurement. Part (b) shows normalised PCE recorded over 1500 hours for one device having particularly high stability. Bulb symbols represent breaks in the measurement due to the lamp being restarted or replaced. Calibrated current-voltage measurements (circles) were taken at 0 hours (black), 150 hours (blue) and 1500 hours (red). The result of these measurements is shown in part (c); $J-V$ sweeps and part (d); stabilised power outputs. Dashed and solid lines represent forward and reverse $J-V$ sweeps respectively.

	After Encapsulation	After 150 Hours Aging	After 1500 Hours Aging
PCE [%] (<i>Stabilised</i>)	13.21 (12.8)	14.52 (14.1)	11.98 (11.7)
J_{sc} [mA/cm ²]	17.18	17.50	16.25
V_{oc} [V]	1.07	1.10	1.09
FF [%]	72.01	75.42	67.87

Table 3: Performance metrics for champion PSCs recorded at three points during 1500 hours aging (data taken from Figure 6a).